Near Surface Geophysics, 2005, 245-257

Seismic prospecting in archaeology: a 3D shear-wave study of the ancient harbour of Miletus (Turkey)

Susanne Woelz* and Wolfgang Rabbel

Institute of Geoscience, Christian Albrechts University Kiel, Otto-Hahn Platz 1, 24118 Kiel, Germany

Received April 2004, revision accepted April 2004

ABSTRACT

A 3D multicomponent shear-wave survey was performed in the area of the ancient city of Miletus (western Turkey). To achieve high spatial resolution of near-surface targets, data were acquired with a geophone array of 1 m grid spacing. The survey served: (1) to investigate archaeologically important details of the basement of one of the silted harbours of Miletus, and (2) to evaluate the potential of close-meshed shear-wave seismics for shallow high-resolution prospecting in a more general sense. Methodically, we could show that isotropic radiation patterns of compressional shear- and surface waves can be reconstructed with simple vector arithmetic even if hand-driven hammer blows are applied as a horizontal seismic source. Presenting time-slices of S-wave propagation, we demonstrate that side-swipe may significantly affect the propagation of refracted waves. It is shown that the wavefronts of surface waves may be far from circular in the case of typical near-surface lateral heterogeneity. As a further phenomenon of wave propagation, we could visualize the coda of a ground-coupled air wave probably caused by mud cracks. Regarding the archaeological background of our study, we could show that the basement of the Milesian Lions' Harbour is shallow enough to provide appropriate ground for ancient construction work. However, by 'true 3D' refraction mapping, we could image small-scale topographic details of the harbour basement, proving that no large ancient stone walls are hidden under the ground. Magnetic anomalies were found to coincide with a lateral increase in Rayleigh-wave velocity. The rectangular shape of this velocity contrast may indicate the remnants of an artificially shaped rock platform or an embankment. Spectral analysis of the surface wavefield shows that this seismic anomaly will be found at a depth of 3–6 m.

INTRODUCTION

In near-surface prospecting, seismic refraction measurements are usually performed along linear profiles, implying that the subsurface structure to be investigated is more or less two-dimensional. However, seismic-wave propagation is a 3D phenomenon, especially when geological interfaces show complicated topography, for example, strong curvature and unknown dip and strike azimuths. In this case, the interpretation of 2D refraction seismic sections can be ambiguous or even wrong. Consideration of the 3D nature of shallow seismic prospecting is of particular importance if seismic shear waves are applied in order to increase the spatial resolution of a survey. If P- and S-wave signals are generated at the same frequency interval, shear waves will show about two-to-ten-times higher resolution than P-waves because of their lower propagation velocity. V_P/V_S ratios even higher than ten are not unusual in a shallow environment. In addition and in contrast to compressional waves, the S-wave velocity V_S is nearly independent of the water saturation of the pore space, so V_S is linked more closely to lithology than V_P (e.g. Stümpel *et al*. 1984). This observation is of particular practical importance if the target of investigation is a shallow horizon slightly below the groundwater table. The groundwater table is associated with an increase in P-wave velocity causing: (1) a P-wave refraction interfering with the target refraction, and (2) a shift of the critical point and the takeover-distance of the target refraction to large offsets. In contrast, the propagation of horizontally polarized S-waves (SH-waves) is not influenced by the groundwater table, so the target horizon may be observed clearly and usually at smaller offsets than the corresponding P-wave refraction. The field procedures for investigating 2D subsurface structure with P- and SH-waves are similar to each other. However, if the subsurface shows a pronounced three-dimensional structure, S-wave acquisition requires more effort than P-waves because the vector character of particle movement and wave propagation has to be considered on both the source and the receiver sides. Depending on the spatial arrangement of source- and receiver-points, layer geometry and source type, geophones will record a mixture of P-, S-, Rayleigh- and Love-waves. The resulting interference pattern may have a confused appearance especially at near-source–geophone offsets as they

* swoelz@geophysik.uni-kiel.de

are usually applied in shallow prospecting. To enable wavefield separation, data have to be recorded in at least two horizontal components or, even better, three components. Thus, adequate geophone orientations for each wave type can be simulated computationally after acquisition. In shallow shear-wave surveys it has become common practice to generate S-waves with a horizontally orientated vector source such as a horizontally wielded sledge hammer. In 2D surveys, the impact source and geophone line will be orientated parallel and perpendicular to the strike of the geological structure, respectively, so preferably SH- and Love-waves are recorded along the profile, and P-energy is minimized. Transferring this concept to 3D means that two orthogonally orientated horizontal sources have to be applied and recorded independently. An optimum source orientation has to be found computationally after the measurements for each geophone position. Here, we intend to demonstrate the potential of shallow 3D multicomponent data by showing two high-resolution data sets recorded using the technique described above. We restrict our analysis to four components (4C-seismics) involving two horizontal source components and two horizontal geophone components.

The field data were acquired in the ancient city of Miletus on the west coast of Turkey (Fig. 1) as part of a project to derive geological boundary conditions for the ancient civilization and insights into other human activities like trade and transport. The focus of this paper, however, is not on the archaeological outcome of the geophysical measurements but on the experience gained with acquisition, processing, visualizing and interpretation of 3D wavefields in the shallow subsurface.

The paper is organized as follows: firstly, we give an overview of the area of interest, including some archaeological and geological information and previous geophysical surveys; secondly, data acquisition, vector processing and visualization techniques are explained; thirdly, we consider the radiation patterns, refracted S-waves and Rayleig waves that can be observed clearly in a 3D data volume; finally, the results are discussed.

ARCHAEOLOGICAL, GEOLOGICAL AND GEOPHYSICAL SETTINGS

Archaeological situation

In ancient times, Miletus was one of the largest, most important and prosperous cities on the coast of Asia Minor. It was situated on a former peninsula in the Latmian Gulf, which today is silted up completely by the sedimentation of the Büyük Menderes (Maiandros) River (Kleiner 1968). It is now stranded 10 km

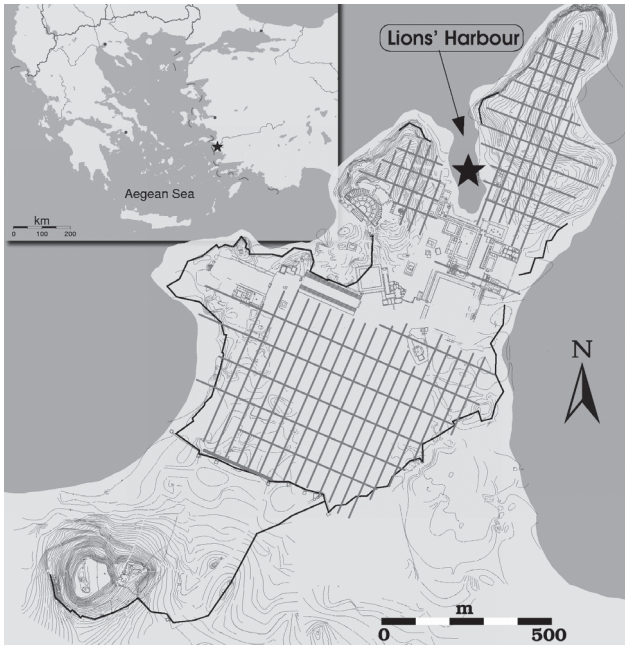

FIGURE 1

Map of the Aegean region inset in the upper left-hand corner with the location of Miletus near the western coast of Turkey indicated. The enlargement shows a former reconstruction (after Kleiner 1968) of the ancient city in Hellenistic times with a few buildings (theatre, market square), parts of the known city wall and the street system. The Lions' Harbour (indicated by star) is located on the north-western side of the city and is incised deeply into the peninsula. This naturally formed, limestone bay is especially suited to serve as a harbour.

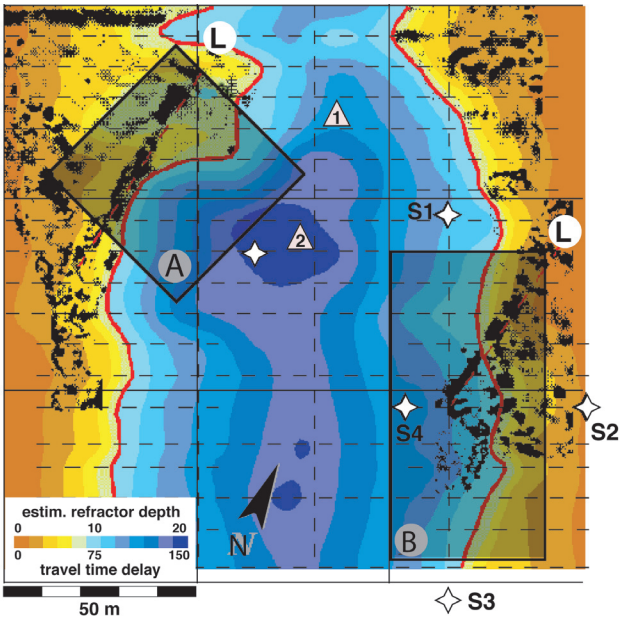

FIGURE 2

Contour map of the basin topography of the Lions' Harbour, based on linear seismic profiling with shear waves (dashed lines). The positions of the lion sculptures are indicated by the letter L. Partly underlying is a grey-scale magnetic map with strong linear anomalies pointing from the sculptures to the south. These anomalies are assumed to be quay walls or mole foundations of the former harbour. Two drilling locations are marked by triangles. A and B indicate the positions of the two dense geophone arrays of the 3D shear-wave survey. Shotpoints are marked with white stars.

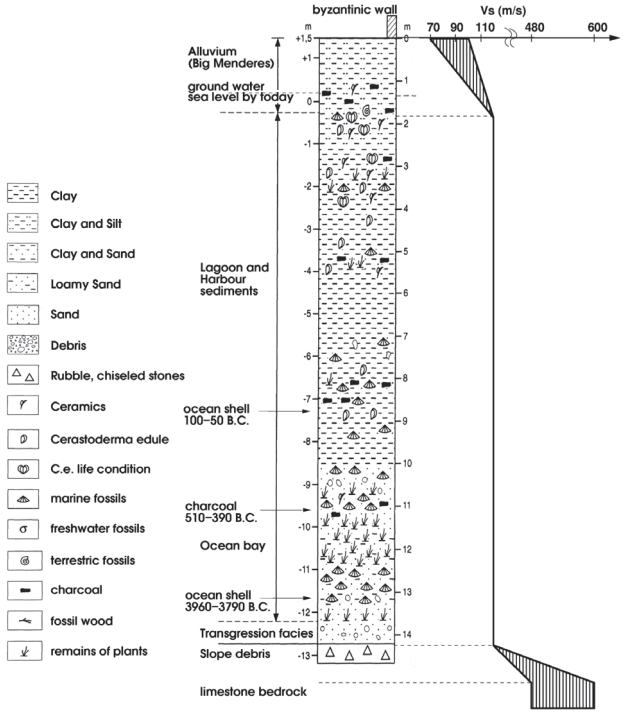

FIGURE 3

Core log containing information on the sedimentation of the Lions' Harbour with implications for the progradation of the Menderes River Delta (after Brückner 1996). The shear-wave velocity profile of Lions' Harbour is shown on the right.

inland. Since Miletus was the centre of Ionian trade, the ground plans of the harbour buildings and basins are of special importance for the architectonic reconstruction of the city. The 3D data sets, the subject of this paper, are from the area of the so-called Lions' Harbour, the basin topography of which was investigated seismically in order to define constraints for a virtual city reconstruction. The harbour is named after two huge lion statues, which are still to be found in the former harbour area (Fig. 2), and it is considered to be one of the archaeological key areas near the city centre.

Geological situation

The Lions' Harbour is located in the north-western part of the city (Fig. 1). It is a former bay of 150×300 m extent. It cuts deeply into the peninsula, separating two Neogene limestone hills, the Homeytepe and the Kaletepe, in the NE and SW, respectively. These hills are part of the Nergiztepe formation reaching up to 110 m thickness, so the previous harbour basin is embedded in limestone (Bay 1996). The axis of the Lions' bay strikes nearly N–S. In the north, an artificial dam is located to prevent the bay from being flooded by the Menderes River. Morphologically, the boundary between the limestone and the sedimentary fill forms an edge of terrain around the whole bay. Approximately half of the bay is covered by a layer of debris, up to 1.5 m thick, from former excavations (Tuttahs 1995).

The basin fill was investigated by drilling at two sites (triangles 1 and 2 in Fig. 2) where the limestone bedrock was found at 12 m and 21 m, respectively. Both sites show similar stratigraphy (see Fig. 3). The Neogene limestone is truncated by an erosional unconformity. Erosional slope debris of limestone (up to 1 m) was found close to the bottom of the bay. Upwards, the log comprises marine, lagoon and harbour sediments with shells, charcoal, remains of plants and human artefacts, i.e. ceramics. From top to bottom the basin fill is rich in clay. Brackish groundwater is found at approximately 1 m depth.

A shear-wave velocity–depth profile derived from refraction and vertical seismic profiling is shown in Fig. 3 (right) (after Stümpel *et al*. 1999). Extremely low S-wave velocities of 70–100 m/s and a strong vertical velocity gradient of 10–25 (m/s)/m are found at the earth's surface. Below 2 m depth, the basin fill shows a constant velocity of about 120 m/s, which is low compared to values quoted in the literature (e.g. Schön 1996). The next horizon is the limestone bedrock on which were the foundations of ancient buildings. Its S-wave velocity of 450–600 m/s shows that it was weathered before sedimentation began. This limestone layer crops out at the boundary of the harbour basin. The drill cores proved that sedimentation was slow until the first century BC and became more rapid in Hellenistic and Roman times. Not later than in Byzantine times, the harbour environment had become swampy and the harbour was useless. The geological profiles are representative of the geological situation all over the area (Brückner 1996, 1998, 2003; Brückner *et al*. 2002).

Previous geophysical surveys

The most important results of a magnetic survey of the harbour and adjacent areas are two diffuse elongated anomalies inside the present morphologically defined basin zone. They are 50 m long, parallel to each other and situated close to the eastern and western harbour boundaries. These anomalies have been attributed to the remnants of former mole foundations or quay walls because they seem to lead straight from the ancient city centre towards the lion monuments, and because they are parallel to the ancient Milesian street system (see Fig. 1) (Stümpel *et al*. 1997).

Attempts to verify these monuments by electromagnetics and ground-penetrating radar failed because of the high electrical conductivity of the clayey and brackish subsoil. Therefore, quite unusually in archaeological prospecting, we applied shear-wave seismics in order to determine the ancient coastal morphology and the topography of the harbour basin.

The choice of shear-wave refraction profiling was motivated on the one hand by the strong contrast in S-wave velocity between basin fill and basement, guaranteeing short critical distances, and on the other hand by the high V_P/V_S ratio providing higher spatial resolution in S-waves than in P-waves.

The major result of 2D S-wave refraction profiling performed along lines nearly perpendicular to the suspected basin axis is

shown in Fig. 2. The basin has asymmetric depth contours with a depth maximum of about 22 m located between the two magnetic anomalies under investigation. The solid line in Fig. 2 is an assumed ancient coast line at about 6 m depth, following a contour line of the seismic depth map. Obviously the topography contours do not match the strike direction of the magnetic anomalies (Stümpel *et al*. 1999; Bruhn 1998).

In order to clarify whether or not these discrepancies between magnetics and seismics are caused by 3D side-swipe effects and because we were principally interested in the small-scale resolution potential of seismic shear waves, we decided to perform two 'true 3D' S-wave surveys. They cover two large areas, 50×50 m and 40×80 m, which include the magnetic anomalies (A and B in Fig. 2, respectively).

DATA ACQUISITION AND PROCESSING

This section describes S-wave data acquisition carried out on the two areas, A and B, covering the magnetic anomalies (Fig. 2), and the processing steps applied in order to separate the intermingled wavefields.

Data acquisition

Measurements in areas A and B were performed with a 48-channel BISON seismograph and a 60-channel Geometrics seismograph, respectively. A sketch of the acquisition layout is shown in Fig. 4.

Geophones were arranged in areas A and B with 1 m grid spacing along linear profiles comprising 48 and 60 sensors, respectively. After each shot sequence, the sensors were moved to the next line, the shot sequence was repeated, and so on, until all profiles were recorded.

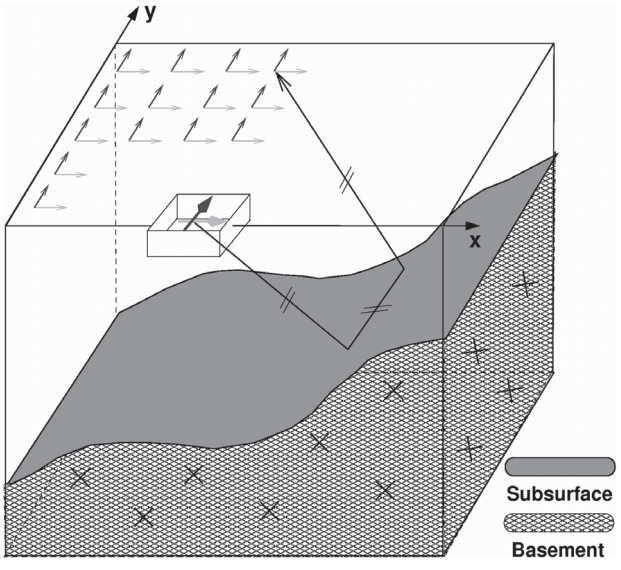

FIGURE 4
Sketch of data acquisition and definition of the acquisition coordinate system.

In area A, we applied single horizontal geophones orientated parallel to the grid coordinate axes (Fig. 4). In area B, three-component Gal'perin-geophones were used, the records of which were transformed computationally to the same grid-parallel coordinate system. Problems in geophone coupling were caused by deep mud cracks originating from flooding during winter, lack of rain during spring, and the hot summers in this region. Figure 5 shows a photograph of these cracks.

Vector data recording of the two horizontal components was complemented by a two-component (2C) vector source: the seismic waves, preferably S-waves, were generated with a hand-held sledge-hammer applied horizontally to the face of a small rectangular pit where a metal plate had been installed vertically. Hammer shots were performed in two orthogonal directions in

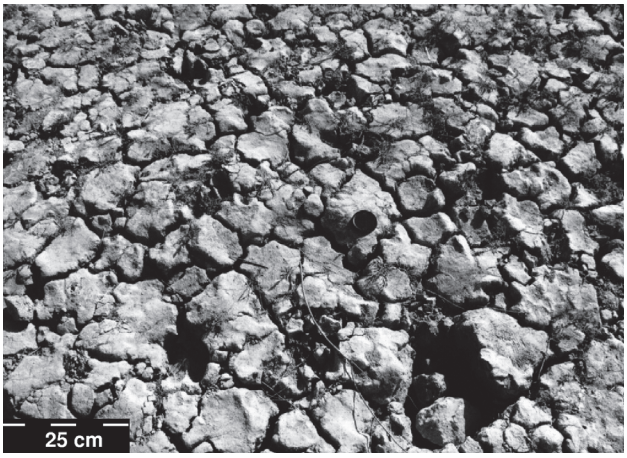

FIGURE 5
Photograph of mud cracks found in area B during the survey. The cracks may cause bad receiver coupling and a coda of ground-coupled air waves (cf. Fig. 16).

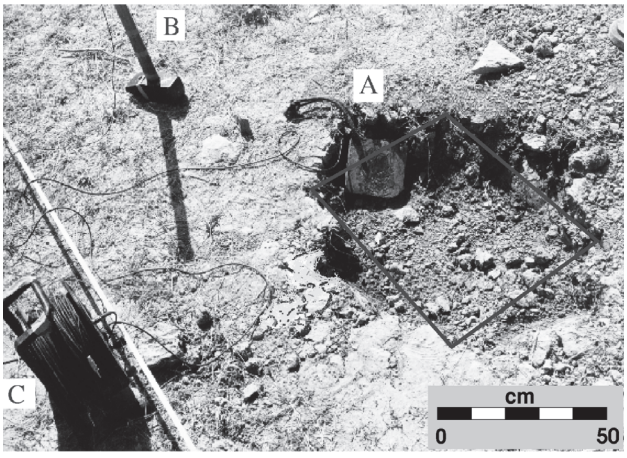

FIGURE 6
Photograph of a source-point after intensive wave excitation. A: Vertical metal plate in a rectangular pit with originally near-vertical walls; B: sledge-hammer with 'accelerometer' for triggering the recordings; C: connecting cable.

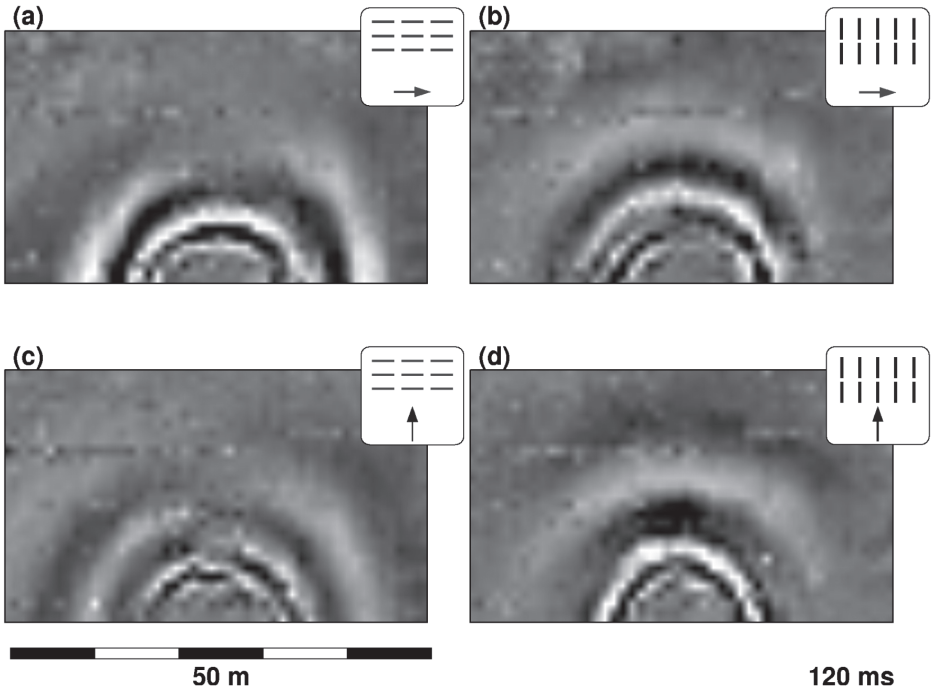

FIGURE 7
Time-slices (120 ms) of original data from area A showing all four horizontal source and geophone combinations. (a) and (b) source in *X*-direction, (c) and (d) source in *Y*-direction; (a) and (c) receiver in *x*-direction, (b) and (d) receiver in *y*-direction (see pictograms). Note that the vertical lines at the centre of the time-slices in (a) and (d) are equivalent to 'SH'- and 'SV'-spreads, respectively.

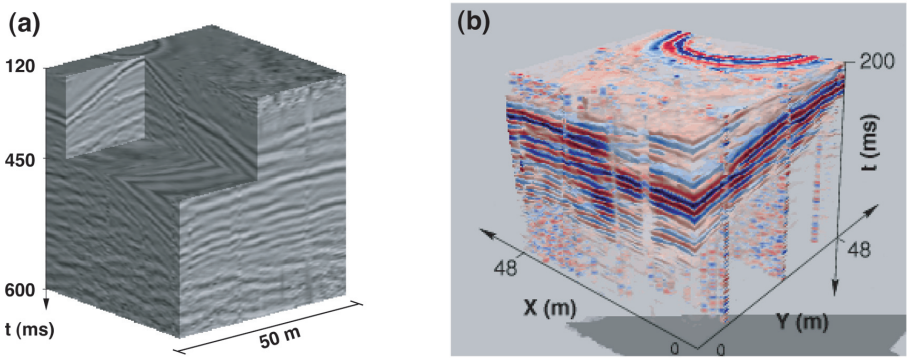

FIGURE 8
(a) Volumetric view of data set A with different cut-outs representing two-dimensional subspaces, such as time-slices, in-line and cross-line sections. (b) The same data volume with amplitude representation (values close to zero are nearly transparent). Top time-slice is at 200 ms.

order to excite all possible horizontal shear-wave components (Fig 6).

In the following, geophone lines, geophone components and hammer shot orientations are labelled with *X* or *Y*, following the grid coordinate system, as illustrated in Fig. 4.

The data were recorded with a recording length of 1 s and a sampling rate of 1 ms. The total data volume amounts to about 1GByte. Due to a good signal-to-noise ratio, two-fold vertical stacking was sufficient.

Data processing

The application of each two horizontal source and geophone components (4C) provides us with four seismic data sets for each investigation area, representing the records of the different source–geophone pairs (Fig. 7). Wavefields recorded with a two-dimensional geophone spread can be presented as data blocks or data cubes (Fig. 8a). Such data blocks combine two spatial coordinates (x and y) with a temporal coordinate (t) and thus they represent the extension of the usual seismogram ($U(x,t)$) into a two-dimensional seismogram ($U(x,y,t)$).

Although data may be represented in 3D views as more or less transparent cubes (Fig. 8b), we found it necessary to combine various 2D sections during interpretation, for example, in-line ($U(x_0,y,t)$), cross-line ($U(x,y_0,t)$) or radial seismogram section ($U(x,y(x),t)$) and time-slices ($U(x,y,t_0)$), which form two-dimensional subspaces of these blocks. The volumetric view of one of the data cubes of area A gives an impression of the spatial interference of body and surface waves (Fig. 8).

Since time-slice sequences are better suited to understanding the spatial and temporal connection between propagating wavefields than volume displays, we display data mainly as time-slice sequences in the following.

Besides some weak band-pass filtering, the major processing step applied in this study consists of vector arithmetic operations

in order to find suitable source and receiver orientations for the wave types considered.

Whereas the seismic acquisition system has a Cartesian geometry, the propagating wavefronts show a rather spherical or cylindrical symmetry. Also the particle displacement deviates from the acquisition coordinate system because it is determined by the local orientation of the wavefront and the wave type considered. As a result, different wave types combine quite differently into the individual geophone components. Therefore, in order to assist interpretation, the geophone components have to be rotated virtually into a spatially variable coordinate system following the local orientation of the wavefronts. In this study, we assumed that the wavefronts are nearly circular with respect to the source point. In a strict sense this cylindrical symmetry is applicable only to wave propagation in 1D media, but our data examples show that it may be a reasonable first-order approximation even in 3D media, if lateral heterogeneity is moderate.

The recording of two orthogonal source and geophone orientations enables us to simulate any source and geophone orientation by elementary vector operations, such as vector addition and rotation of the coordinate system.

Let $u_x^Y(t)$, $u_x^X(t)$ and $u_y^Y(t)$, $u_y^X(t)$ be the four time series recorded for each geophone location, where X and Y are the respective shot orientations, and x and y are the geophone orientations. Using equation (1) below, we can compute the virtual records of shots X and Y for an arbitrary horizontal geophone orientation corresponding to angle in the (x,y)-coordinate system:

$$\begin{pmatrix} u_\alpha^Y \\ u_\alpha^X \end{pmatrix} = \begin{pmatrix} \cos\alpha & \sin\alpha & 0 & 0 \\ 0 & 0 & \cos\alpha & \sin\alpha \end{pmatrix} \begin{pmatrix} u_x^Y \\ u_y^Y \\ u_x^X \\ u_y^X \end{pmatrix}. \quad (1)$$

To simulate, in addition, a horizontal hammer shot B orientated at an angle β in the (x,y)-system, we have to apply equation (2) below to the result of equation (1):

$$u_\alpha^B = \cos\beta u_\alpha^X + \sin\beta u_\alpha^Y. \quad (2)$$

Equations (1) and (2) are applied to our data sets in order to simulate individual shot–geophone orientations for each geophone location corresponding to 'transverse' and 'radial' configurations. 'Transverse' and 'radial' refer to a shot-and-geophone orientation perpendicular and parallel to the observation azimuth, respectively. In the transverse configuration, for example, the receivers are orientated tangentially to circles around the shotpoint, and the source is positioned parallel to each receiver. This case corresponds to a rotated cylindrical source creating pure SH- and Love-waves if the media were ideally 1D. In the radial configuration, source and receiver are arranged parallel to an imaginary connecting line between the source point and a receiver point. In this case, the source acts like a horizontally exploding ring generating P-, SV- and Rayleigh-waves in 1D media. (In all figures, source and geophone orientations are indicated by pictograms.) Although derived from 1D media, both configurations simplify the interpretation of the recorded wavefield, and also often in 3D media if raypaths do not bend too strongly in the horizontal plane.

In the following, we apply this vector rotation technique in order to investigate three aspects of wave propagation: the radiation pattern of the applied horizontal hammer source and the lateral refraction of SH-waves and Rayleigh-waves.

WAVEFIELD PHENOMENA

To demonstrate the reason for our experiments, we present time-slices showing the partly complicated structure of the recorded wavefields. This complexity is partly caused by the basin topography and partly by irregularities in the near-surface layer.

To give an overview, Fig. 9 shows a sequence of time-slices for data recorded in area A. The data is rotated to a transverse geometry (equations (1) and (2)) as indicated by the pictogram in the first time-slice at 30 ms. Subsequent time-slices are separated by time steps of 30 ms. In order to enhance weak arrivals at later recording times and larger offsets, the data was plotted using an AGC of 200 ms window length. In order to correlate the distinct kinematic and dynamic features of the wavefield with other geophysical information available for the area, the figure also displays grey-scaled magnetic data and a subsurface model as derived from 2D refraction seismics.

The direct wave has approximately radial symmetry and coherence (time-slices at 60–180 ms), as we would expect in the case of a homogeneous half-space. However, its wavefront becomes increasingly deformed as it approaches the shallower zones of the basement.

We observe a weak refracted wave travelling from left to right, starting at 210 ms right below the upper left-hand corner. It is not connected to the direct wave. At about 300 ms it merges with a more obvious refraction, appearing at 270 ms in front of the direct wave (see also the broad white phase in the time-slice at 300 ms). The nature of this refraction will be investigated in the next section.

A prominent surface wavefield showing dispersion follows the refraction (time-slices 330–540 ms). Like the direct wave it deviates slightly from radial symmetry (540 ms). This is caused by the decrease in refractor depth towards the upper left-hand corner of the area (see subsurface model). This effect is even more pronounced in area B and will be discussed in more detail in the last subsection.

The SH-reflection from the basin bottom starts at about 240 ms and is slightly shifted to the left as a result of the sloping basin.

From 420 to 510 ms, we can observe a strong surface-wave reflection starting in the lower left-hand corner and travelling 'backwards', from left to right. Its origin cannot be determined but it suggests that the slope of the basin is possibly greater than in the smoothed subsurface model derived from 2D seismics (side reflection).

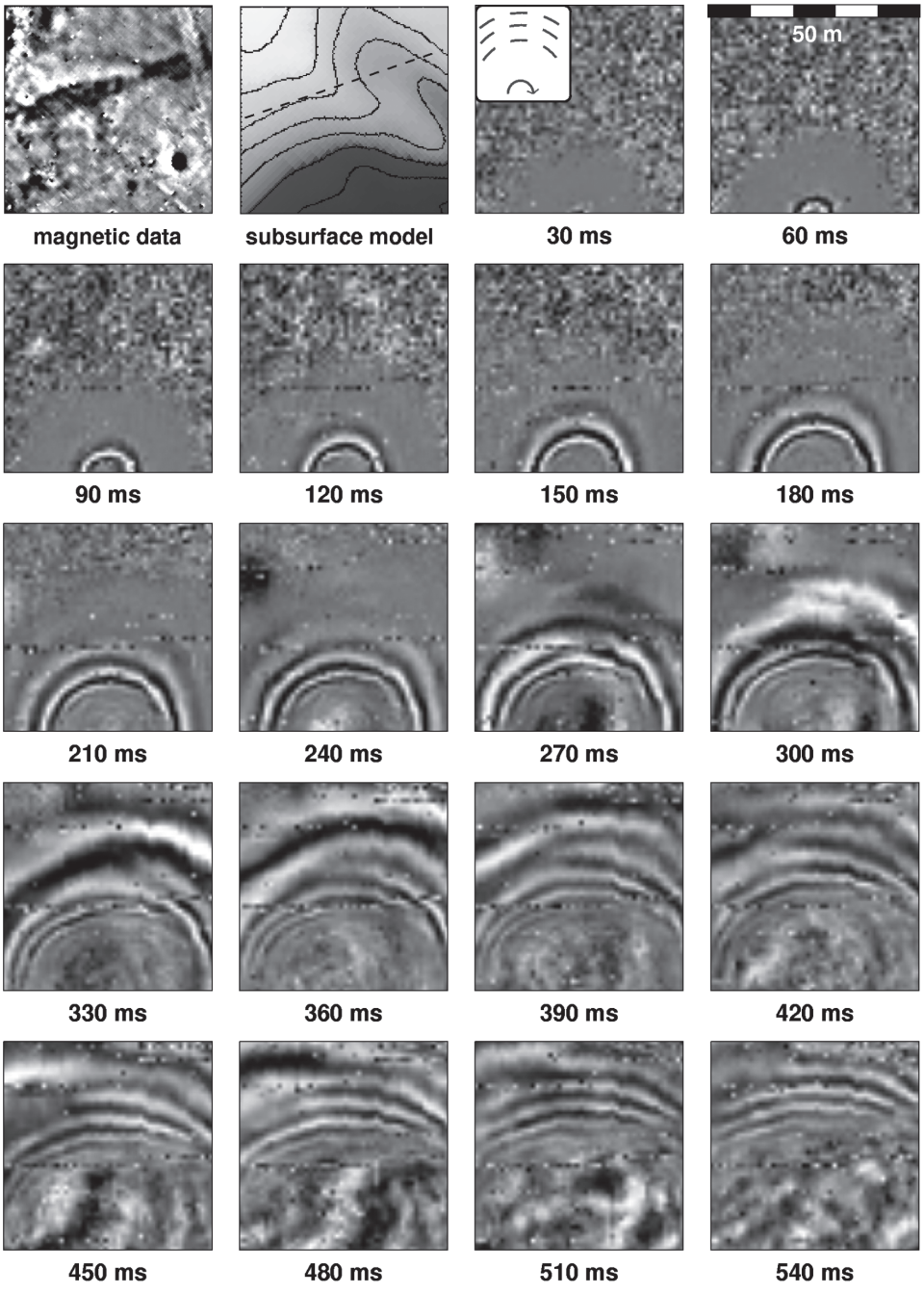

FIGURE 9
Time-slice sequence in numerically reconstructed transverse acquisition geometry of area A. The virtual source can be regarded as a cylindrical rotation source. Each geophone is virtually orientated transversely to the source direction (see the pictogram in the upper row, first seismic time-slice at 30 ms). Time-slices are shown from 30 ms to 540 ms in steps of 30 ms. The upper row also shows magnetic data and a subsurface model derived from 2D refraction seismics with contour lines at 2 m intervals.

Radiation patterns

Our three-dimensional four-component seismic measurements provide the possibility of studying the radiation pattern of the source. This investigation serves to verify whether or not our hand-driven hammer source behaves like a vector point source even if its shape is far from being a point. This deviation could be expected to increase with progressive destruction of the soil caused by repeated hammer blows during the experiment (see Fig. 6).

Amplitude fields recorded for four different source–receiver combinations in area A are shown in Fig. 7(a–d). Source and receiver orientations are symbolized in the insets by arrows and dashed lines, respectively. The amplitude fields represent the interference patterns of at least four, possibly five, different wave types: SH- and SV-type shear waves, Love- and Rayleigh waves, plus some weak remnants of the direct P-wave travelling in the narrow land velocity zone above the groundwater table. Because of the Cartesian arrangement of the receivers, waves of different polarity intermingle so that the individual wave types can be hardly distinguished. The situation improves after the receivers have been rotated to radial and transverse orientations (i.e. equa-

tion (1) is applied). The outcome of this operation is shown in Fig. 10. Panels (a) and (b) show the wavefield as recorded by transversely and radially orientated geophones, respectively, after excitation in the *x*-direction. The analog for a vector force in the *y*-direction is shown in panels (c) and (d). These displays illustrate the source radiation patterns for the transversely and radially polarized wavefields. It is unusual that an expected phase reversal in panel (b) is not observed. A simplified test of source radiation is finally achieved by applying equation (2) to transform the data to complete transverse and radial configurations (Fig. 10(e) and (f), respectively). After this operation, amplitudes appear well equalized along the wavefronts, indicating that the hammer source worked reasonably well despite all deviations from an ideal point source. The dashed circle in Fig. 10(e) shows the front of direct SH- and Lov waves. Comparison of adjacent time-slices (cf. Fig. 9) shows that these fronts move with a velocity of approximately 90 m/s. In the radial configuration time-slice (Fig. 10 f), significant energy is found outside the circle, which has to be attributed to a direct P-wave travelling with a velocity of about 250 m/s in the partially saturated zone above the groundwater table. In addition, the asymmetry inside the dashed circle (Fig. 10) shows that the basin fill is heterogeneous.

Another example of small scale heterogeneity within a radiation pattern can be detected in area B. Figure 11 shows rotated data of area B at four successive times at intervals of 20 ms. Transverse (left) and radial (right) configurations are plotted together in one panel. The shotpoint is located within the grid (diamond in Fig. 11, cf. Fig. 2). This example confirms the point-source character of the hammer source and shows that the wavefront has nearly perfect radial symmetry (dashed line). Small-scale deviations from this symmetry are partly due to geophone gridding, which is partly larger than the grid spacing, an effect we relate to the existence of pronounced mud cracks in this area (Fig. 5). Note that the P-wave velocity of the vadose zone is even lower than in area A (140 m/s).

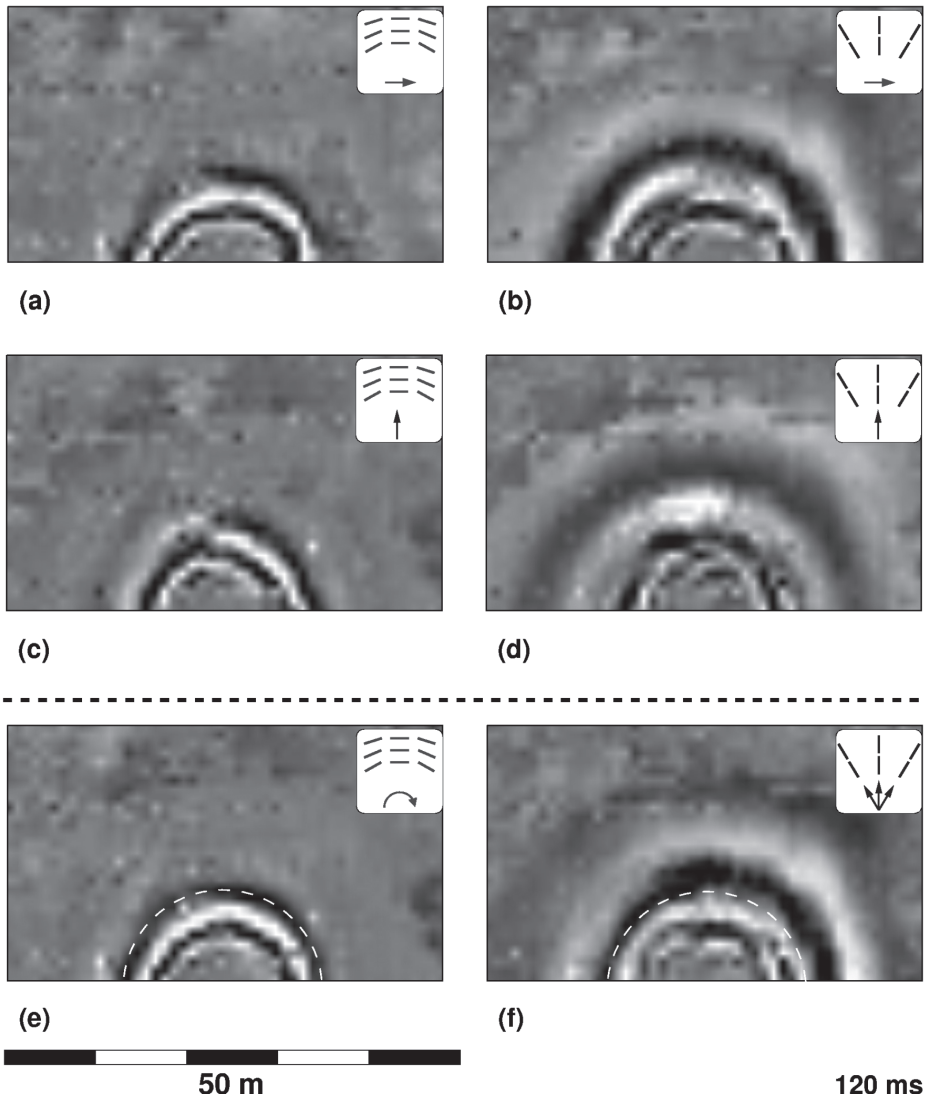

FIGURE 10
Time-slices (120 ms) of six data sets from area A after application of equations (1) and (2), corresponding to virtual geophone and source rotations, respectively. Panels (a) and (b): wavefield as if recorded by transversely and radially orientated geophones, source direction parallel to the *x*-direction. Panels (c) and (d): the same for a source orientated parallel to the *y*-direction. Panels (e) and (f) show the transverse and radial geometry after orientating the virtual shot components perpendicular and parallel to the tie-line of source and geophone, respectively. The dashed circle indicates the wavefronts of the direct SH- and Love-waves (e). In panel (f) significant energy is found outside this circle which can be attributed to the direct P-wave travelling in the partially saturated zone above the groundwater table.

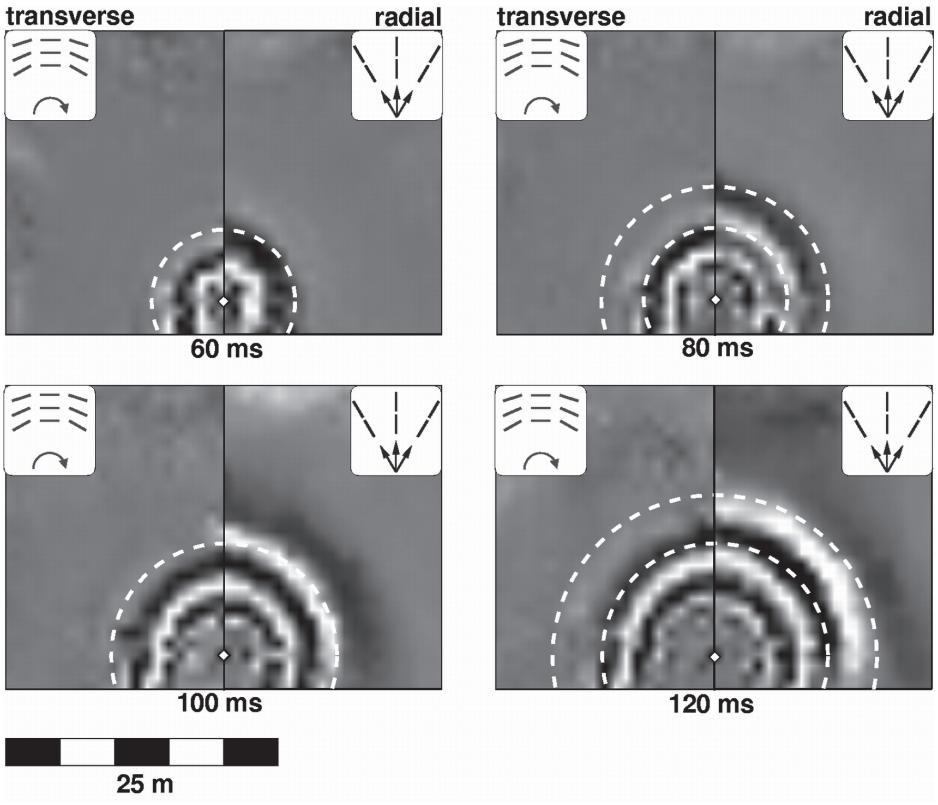

FIGURE 11
Time-slices from data set B at four successive times (60, 80, 100 and 120 ms). In each time-slice the transverse geometry is shown on the left-hand side and the radial geometry on the right-hand side (see pictograms). White dashed semicircles indicate wavefronts corresponding to a homogeneous medium. The wavefronts of the field data mostly follow this pattern. Small differences could be explained by anisotropy media. The irregularity of the wavefronts is probably caused by mud cracks (see Fig. 5).

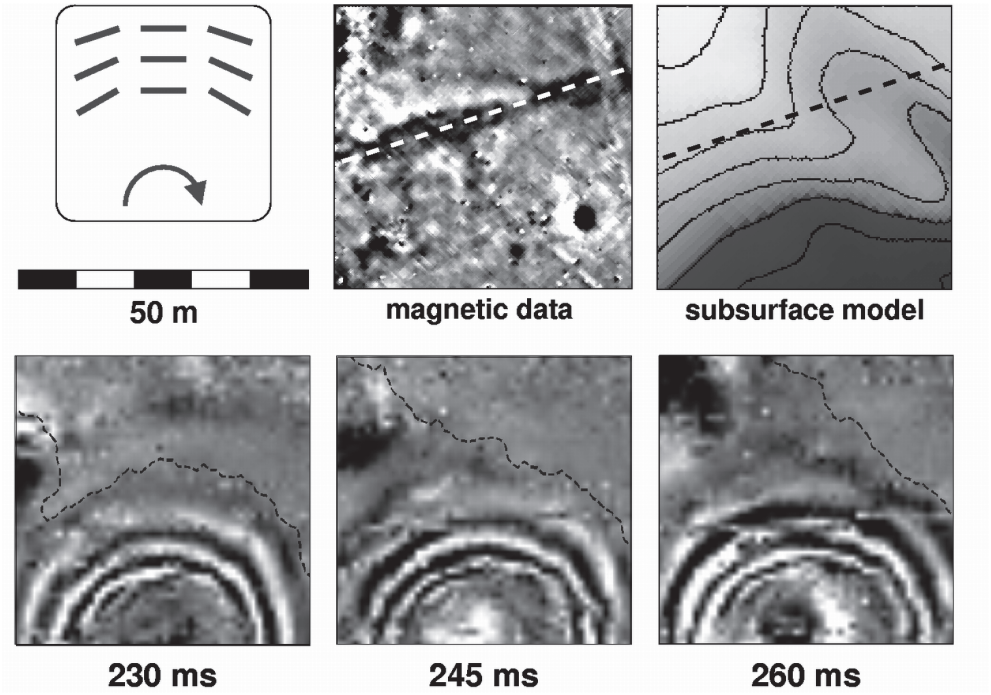

FIGURE 12
Time-slice sequence from data set A showing a refracted wave at 230, 245 and 260 ms corresponding to transverse geometry (pictogram upper left-hand side). The first appearance of the refracted wave is at about 215 ms (not shown) on the upper left-hand corner of the area. Later, at about 230 ms, the refracted wave appears in the middle and on the right side. It seems that both parts merge into one wavefront at about 245 ms. Also shown are the magnetic data and the subsurface model (upper row middle and right-hand side, respectively) of area A.

The velocity of the direct S-wave has not changed from areas A to B (approximately 90–100m/s).

Refracted waves

The curved bedrock topography below area A (Fig. 2) gives us the opportunity to study corresponding distortions of refracted wavefields. The dashed lines in the time-slices of Fig. 12 (lower row) show the approximate position of a refracted S-wave heading upwards along the slope of the ancient Milesian shore (Fig. 12, top right). Obliquely incident wavefronts such as those shown in Fig. 12 are the main error source in 2D refraction seismics.

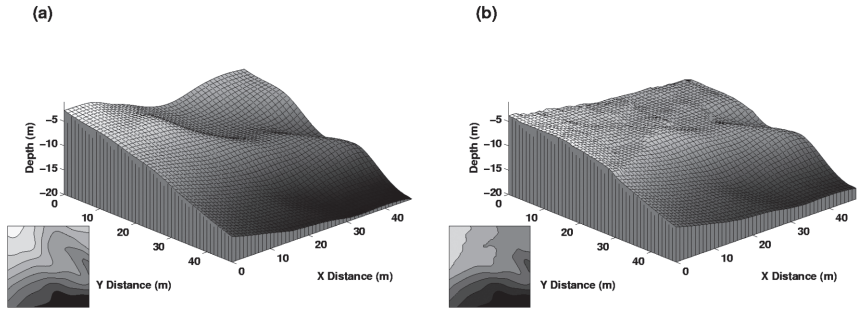

FIGURE 13
Subsurface models for area A as they were used for finite-difference traveltime modelling (cf. Fig. 14). Panel (a) shows a 'pseudo-3D' model derived from parallel 2D refraction lines; panel (b) shows the 'true 3D' model based on the 3D shear-wave survey. The deeper part of model (b) was cloned from model (a). The insets at the lower left-hand corners show contour plots of the models.

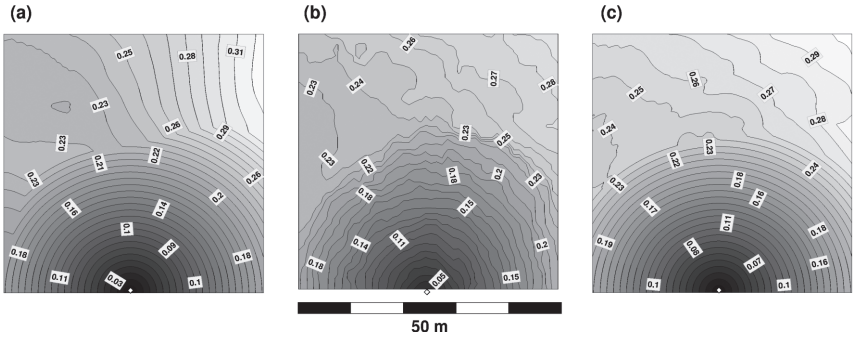

FIGURE 14
(a) and (c) Results of finite-difference traveltime modelling of the pseudo- and true 3D subsurface models of Fig. 13, compared to (b) observed first breaks from data set A.

In order to investigate this effect, we computed first-break traveltimes for two different subsurface models using the finite-difference method, and we compared these synthetics with the observed traveltime field. The first model (Fig. 13(a), cf. Fig. 2) was derived from parallel refraction lines interpreted with a 2D inversion technique. Therefore, it represents a sort of pseudo-3D model. The second model is based on the new 'true 3D' survey (Fig. 13b). In this case, the bedrock topography was reconstructed by applying the delay-time method to the refracted traveltime field, which was observed continuously within the western part of the investigation area (upper part of Fig. 14b). The eastern part of model (b) was cloned from model (a) because this area is masked by the direct arriving wavefield in the 3D survey (lower part of Fig. 14b). The new model (b) indicates that the refractor is flatter than initially assumed. Also, because of the dense geophone grid, the 3D survey reveals more topographic details with a resolution on the metre-scale. For both models, an overburden velocity of 120 m/s and a refractor velocity of 500 m/s were assumed (cf. Fig. 3).

The synthetic first-break traveltime fields corresponding to models (a) and (b) are shown in Fig. 14(a) and (c), respectively. For comparison, the true traveltime field is shown in Fig. 14(b). The traveltime fields of the 'pseudo-3D' and the 'true 3D' models differ mainly in the azimuth of the propagation direction of the refracted arrival (see upper part of Fig. 14). The 'true 3D' model fits the observation almost perfectly (cf. Fig. 14 b with c). In contrast, the 'pseudo-3D' model differs from the observation by up to 10% in traveltime and approximately 45° in propagation azimuth.

Surface waves

To investigate whether or not lateral heterogeneity can be mapped by surface waves, we consider area B where the 'pseudo-3D' model based on linear refraction profiling and 2D interpretation had shown inconsistencies with the magnetic strike lines (Fig. 2). A sequence of time-slices from area B showing propagating Rayleig waves is compared in Fig. 15 with magnetic contours and a geological site sketch. The shot position is indicated by S4.

Soil heterogeneity causes a strong deformation of the originally circular wavefronts (cf. Fig. 11 with Figs 15 and 16). More than 10 m phase advance occurs in the area of excavation debris (lower right-hand corner of Figs 15, 16, left-hand column). Additional phase advance is observed in the upper centre of the figures in an area bounded by the contour of the investigated magnetic anomaly (indicated by a thin white line in Fig. 15). Between 260 and 350 ms, phases propagate at 130 m/s within the area bounded by the magnetic anomaly, i.e. about 50% faster than outside. Also, the dispersion pattern changes abruptly along the magnetic line (very clearly visible in the 320 and 350 ms time-slices in Fig. 15).

A spectral decomposition of data volume B (Fig. 16) shows that the discontinuity of the Rayleigh wavefront is best observed at frequencies between 16 and 32 Hz. At higher and lower frequencies, phases tend again to become more circular (Fig. 16, right-hand column).

Assuming that the apparent wavelength of the spectral components of the Rayleig wave corresponds approximately to their penetration depth, we estimate that the magnetic heterogeneity

should be found at about 3 to 6 m depth. Thus, the 3D Rayleigh-wave analysis shows that a seismic velocity discontinuity is indeed associated with the magnetic anomaly and that this structure was mapped incorrectly by the pseudo-3D refraction survey.

Besides surface-wave behaviour, the spectral decomposition reveals a ground-coupled air wave, observed in the 90 ms time-slice between 126 and 256 Hz (Fig. 16, bottom left). Its front corresponds exactly to a circular wave with a velocity of 330m/s, followed by an irregular coda of about 10 m length. The coda could be caused by acoustic energy trapped in the pore space of the mud cracks (see Fig. 5).

CONCLUSIONS

Discrepancies between magnetic structure and basement contours derived from 2D shear-wave refraction surveys prompted us to test the applicability of 3D multicomponent seismics to shallow high-resolution prospecting. In this case, 'shallow' means a maximum target depth of 20 m, 'high-resolution' means a geophone array of 1 m grid spacing to record shear- and surface waves with an average wavelength of 2–3m. The test site, the silted Lions' Harbour of the ancient city of Miletus, provided us with a lithologically simple situation where structural complexity is introduced by basement topography. Methodically, the following aspects turned out to be important:

- An isotropic radiation pattern of compressional shear- and surface waves can be reconstructed without practical problems by simple vector arithmetic, even if hand-driven hammer blows act as a seismic source. A precondition is, of course, that both horizontal source components are recorded separately on two- or three-component geophones.
- Wavefront bending due to refractor geometry or velocity heterogeneity may be significant. Effects are amplified by the enormous velocity contrast often found in near-surface layers: The comparison between refractor models derived from 'true 3D' acquisition and 'pseudo-3D' acquisition consisting of parallel linear profiles, showed that the refractor is flatter than initially assumed.
- To avoid complications in traveltime interpretation, the geophone coordinate system should be aligned approximately parallel or perpendicular to the wavefronts, leading to transverse or radial acquisition geometries, respectively. Here, we adjusted the coordinate system *ad hoc*, but the bending of wavefronts observed in the data shows clearly that space- and time-variant algorithms are required.
- We were surprised by the richness of geological and archaeological details even below the wavelength limit. Surface waves are able to map sharp lateral material contrast with lower than wavelength accuracy. Even the influence of mud cracks could be imaged in the coda of ground-coupled air waves and radiation patterns.
- Simple time-delay techniques applied to SH-refracted arrivals are capable of mapping coherent basement structures on the metre-scale, which would clearly have been smoothed out as 'noise' if data had been acquired in a coarser grid or along linear 2D profiles.

If acquired in 3D, seismic vector data have the potential to resolve lateral velocity heterogeneity with high resolution. However, due to acquisition geometry and wavefield character-

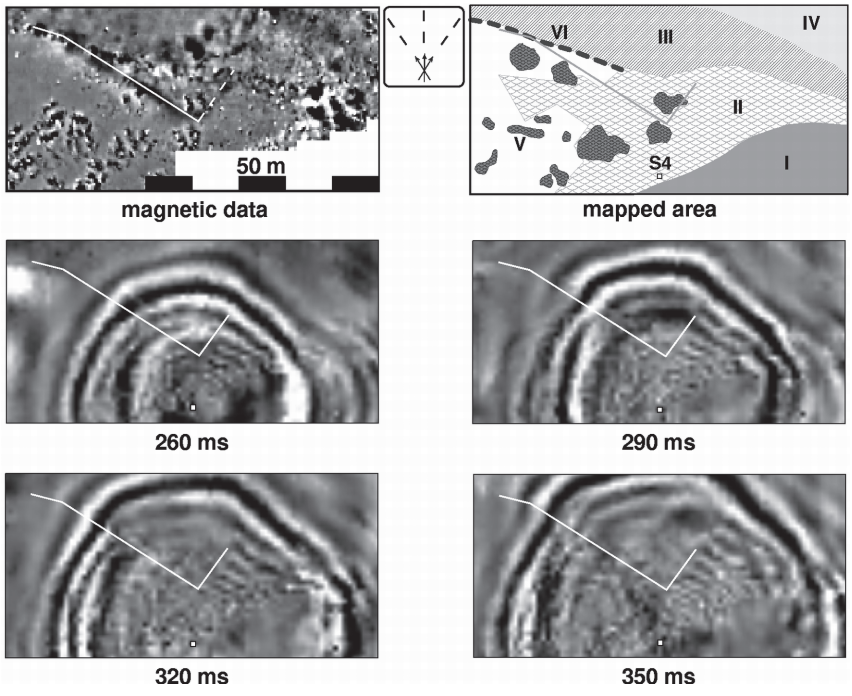

FIGURE 15
Time-slices from data set B at four successive times (260, 290, 320 and 350 ms) compared to the magnetic map on the upper left-hand side and the mapped area on the upper right-hand side (I-excavation debris, II-mud cracks, III-tamarisks roots, IV-slight slope, V-small excavation piles, VI-marble remains). Time-slices correspond to radial geometry. The solid white line marks the position of the magnetic anomaly. The surface waves show a clear wavefront deformation indicating a lateral velocity contrast.

istics, different phases of the wavefield intermingle. Interpretation of S-wave data in 3D is improved if orthogonal horizontal point sources are applied. Simple mathematical vector operations help significantly in the interpretation even of complex wavefields. To avoid complications in traveltime interpretation, the wavefield must be separated, leading to transverse or radial acquisition geometries.

Regarding the archaeological background of our study, we were able to show that the basement of the Milesian Lions' Harbour is shallow enough to provide appropriate ground for the construction of ancient harbour buildings. The ancient moles, possibly indicated by magnetic anomalies, would have been founded on weathered limestone at about 5–6 m depth below the present earth surface. Although this had been largely evident from the basement map derived from linear profiling, important additional information was provided by the 3D S-wave survey.

The 1×1 m grid of geophones revealed small-scale topographic detail. It was shown that no large ancient stone walls, which could be associated with the magnetic anomaly, are hidden under the ground of area A. Therefore, this magnetic anom-

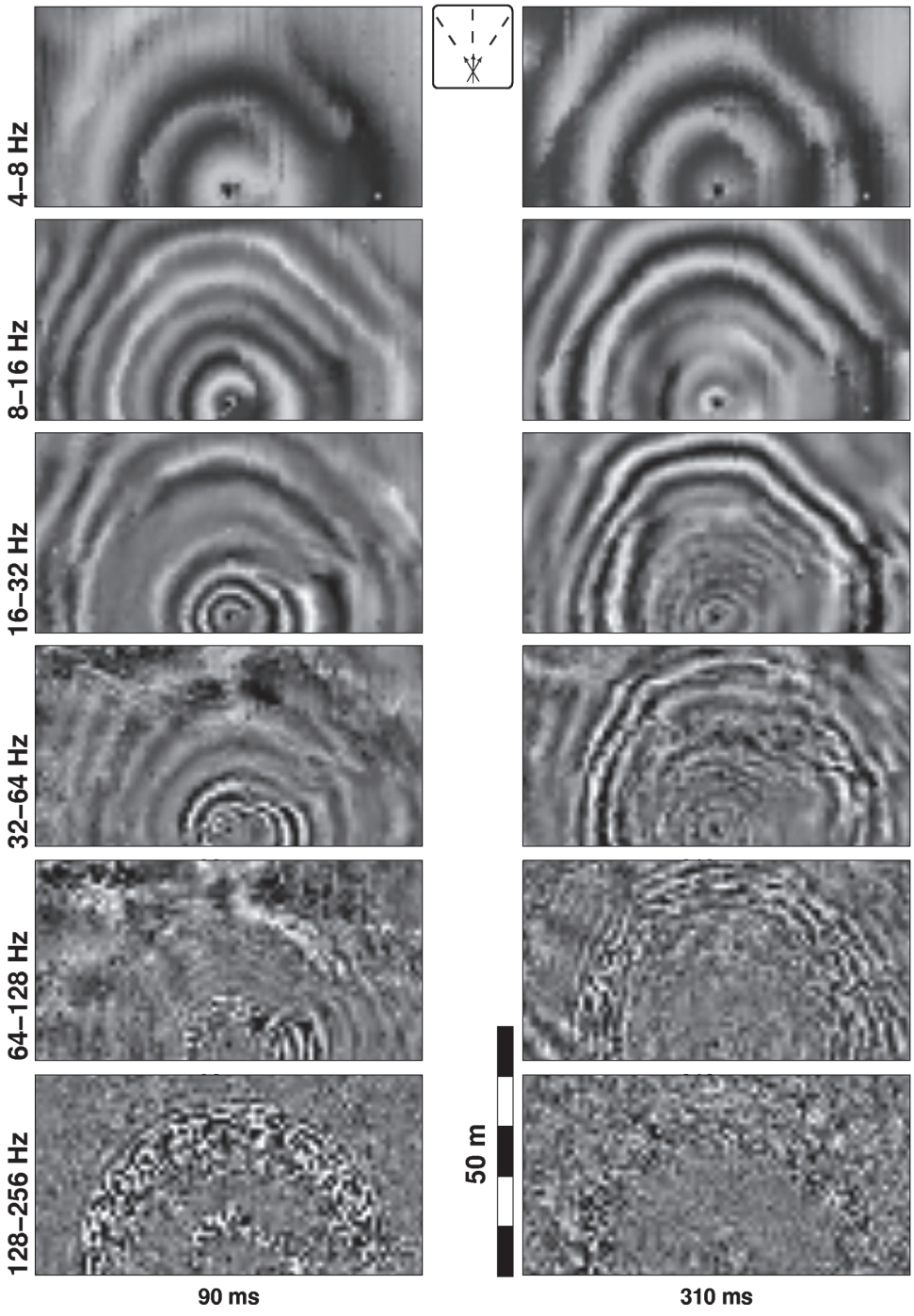

FIGURE 16
Spectral analysis of time-slices from data set B at 90 ms (left) and 310 ms (right). Time-slices correspond to radial geometry. Frequency intervals of an octave band-pass filter are shown on the left-hand side. Note the ground-coupled air wave and its coda at 90 ms and 128–256 Hz.

aly must be caused by small volumes of strongly magnetized material. A candidate for this matter is a local marl, enriched by volcanic ashes, which was applied in ancient times to equalize the ground before construction and to plaster foundation walls.

In area B, the magnetic anomaly under investigation coincides with a lateral increase in Rayleigh-wave velocity. The rectangular shape of this velocity contrast may indicate the remnants of an artificially shaped rock platform or an embankment. Spectral analysis of the surface wavefield indicates that this seismic anomaly will be found at a depth of 3–6 m.

ACKNOWLEDGEMENTS

We are grateful to the German research foundation DFG for funding this project and to the state of Schleswig-Holstein for supporting the research with a scholarship. Support from Harald Stümpel and the Archaeometrie group of Kiel University, V. von Graeve, Ruhr University Bochum, head of excavations in Miletus (Turkey) and Turkish workers is also warmly acknowledged.

REFERENCES

Bay B. 1996. *Das Neogen der Umgebung von Milet*. Diplomkartierung, Universität Bochum.

Brückner H. 1996. Geoarchäologie an der türkische Ägäisküste. *Geographische Rundschau* **48**, 568ff.

Brückner H. 1998. Coastal research and geoarchaeology in the Mediterranean region. In: *German Geographical Coastal Research - The Last Decade* (ed. D.H. Kelletat), 235ff. Institut for Scientific Cooperation, Tübingen, Germany.

Brückner H. 2003. Delta evolution and culture - aspects of geoarchaeological research in Miletos and Priene. In: *Troia and the Troad - Scientific Approaches* (eds G.A. Wagner, E. Pernicka and H.-P. Uerpmann), ch. 9, 121ff. Springer Verlag, Inc.

Brückner H., Müllenhoff M., Handl M. and van der Klaas B. 2002. Holocene landscape evolution of the Büyük Menderes Alluvial Plain in the environs of Myous and Priene (Western Anatolia, Turkey). *Z. Geomorph. N.F.*, Suppl.-Bd. **127**, 47–65.

Bruhn C. 1998. *Wellenfrontenverfahren zur Inversion refraktionsseismischer Daten am Beispiel des antiken Löwenhafens von Milet*. *Diplomarbeit*, Christian-Albrechts-Universität, Institut für Geophysik, Kiel.

Kleiner G. 1968. *Die Ruinen von Milet*. Walter de Gruyter & Co., Berlin.

Schön J.H. 1998. Physical properties of rocks: fundamentals and principles of petrophysics. In: *Handbook of Geophysical Exploration: Seismic Exploration* (eds K. Helbig and S. Treitel), 2nd edn. Vol. **18**. Pergamon Press, Inc.

Stümpel H., Kähler S., Meissner R. and Milkereit B. 1984. The use of seismic shear waves and compressional waves for lithological problems of shallow sediments. *Geophysical Prospecting* **32**, 662–675.

Stümpel H., Bruhn C., Demirel F., Gräber M., Panitzki M. and Rabbel W. 1997. Stand der geophysikalischen Messungen im Umfeld von Milet. *Archäologischer Anzeiger*, 124ff.

Stümpel H., Demirel F., Rabbel W., Trinks I. and Wölz S. 1999. Geophysikalische Prospektion im Umfeld von Milet 1996-1997. *Archäologischer Anzeiger*, 89ff.

Tuttahs G. 1995. Wasserbauliche Problemfelder am Grabungsplatz Milet: Zustand und Aufgaben. *Archäologischer Anzeiger*, 265–275.